Biocompatible 3D Printed MXene Microlattices for Tissue-Integrated Antibiotic Sensing

*Anand P. Tiwari, Sreejith S. Panicker, Julia E. Huddy, Md Saifur Rahman, Katherine R. Hixon, and William J. Scheideler**

Thayer School of Engineering
Dartmouth College, Hanover, NH 03755, United States
E-mail: william.j.scheideler@dartmouth.edu

ABSTRACT

3D continuous mesoscale architectures of nanomaterials possess the potential to revolutionize real time electrochemical biosensing through higher active site density and improved accessibility for cell proliferation. Herein, 3D microporous $Ti_3C_2T_X$ MXene biosensors are fabricated to monitor antibiotic release in tissue engineering scaffolds. The $Ti_3C_2T_X$-coated 3D electrodes are prepared by conformal MXene deposition on 3D-printed polymer microlattices. The $Ti_3C_2T_X$ MXene coating facilitates direct electron transfer, leading to efficient detection of common antibiotics such as gentamicin and vancomycin. The 3D microporous architecture exposes greater electrochemically active MXene surface area, resulting in remarkable sensitivity for detecting gentamicin (10 nM - 1 mM) and vancomycin (100 nM - 1 mM), 1000 times more sensitive than control electrodes composed of 2D planar films of $Ti_3C_2T_X$ MXene. To characterize the suitability of 3D microporous $Ti_3C_2T_X$ MXene sensors for monitoring drug elution in bone tissue regeneration applications, osteoblast-like (MG-63) cells are seeded on the 3D MXene microlattices for 3, 5, and 7 days. Cell proliferation on the 3D microporous MXene was tracked over 7 days, demonstrating its promising biocompatibility and its clinical translation potential. Thus, 3D microporous $Ti_3C_2T_X$ MXene can provide a platform for mediator-free biosensing, enabling new applications for *in vivo* monitoring of drug elution.

Keywords: *3D printed electrochemical sensors; MXene; Antibiotic detection; Biosensing; tissue-engineering scaffolds.*

INTRODUCTION

Aminoglycosides, such as gentamicin, are critical broad-spectrum antibiotics that have been shown to be extremely effective in the treatment of many bacterial infections.[1] The therapeutic and pharmacologic efficacy of these antibiotics has also led to their use in drug eluting biomaterials such as bone graft substitutes[2] and tissue engineering scaffolds (TES)[3–6] as an attractive approach for mitigating infection risk and reducing the need for systemic antibiotic administration. However, proper dosing of antibiotics and control of release kinetics are essential for preventing cytotoxic effects of antibiotics in high concentrations.[7] Recent work in the field of 3D printed biomaterials has shown that 3D micro and macro pore structure design can program the duration and volume of drug elution to provide a degree of control over antibiotic delivery in tissue engineering applications.[8] 3D printing of this class of TES could be particularly useful in applications such as bone tissue regeneration that demand precise control over tissue geometry as well as mechanical properties.[9] However, there is a significant clinical need for better methods to monitor and control antibiotic drug release in these 3D printed implanted biomaterials.

Various *ex vivo* analytical techniques for determining appropriate antibiotic dosage are available such as capillary electrophoresis-mass spectrometry,[10] chromatographic,[11] and spectrophotometric[12] methods to help prevent dangers of excess antibiotics.[13] However, these methods have limited sensitivity, require additional sample preparation, and involve toxic organic solvents.[14] Instead, bioelectronic sensing technologies that could be integrated directly with implantable biomaterials such as TES could provide an ideal solution to real-time, *in vivo* monitoring for guiding new therapies and optimizing survival of implanted tissues. By comparison, electroanalytical potentiometric methods using electrochemical analysis (potentiometric, and amperometry) offer the advantage of easy miniaturization, and accurate antibiotic detection with simple operation.[15] For example, carbon paste electrodes (CPEs) including high surface area carbon nanomaterials (carbon nano tubes, graphene) incorporated with antibiotics ions have been demonstrated with high sensing performance.[16,17] However, limited selectivity of carbon nanomaterials due to lack of functional groups, and hydrophobicity hinder their application in biological samples. In this regard, nanomaterials having functional groups could solve the selectivity issue as well as the wettability issue for enabling higher sensing performance.

MXenes present an emerging set of 2D nanomaterials that offer attractive electronic characteristics for implantable biosensors. MXenes consist of a group of 2D transition metal carbides/nitrides obtained by etching of the A layers from $M_{n+1}AX_n$ (MAX) phases (where M is a transition metal, A is a group 13 or 14 element, and X is carbon and/or nitrogen).[18] Etching the A element results in the formation of functional groups such as OH^-, O^{2-} and F^{1-} on the edge sites

of MXene, boosting hydrophilicity and electrochemical activity.[19] MXenes also possess potential for high density incorporation of several functional groups and their ultrathin 2D sheet-like morphology as well as excellent ion intercalation behavior make them an ideal material for electrochemical sensing.[20] Moreover, MXenes possess excellent biocompatibility, adjustable transverse size, good hydrophilicity, and quick absorption of aromatic compounds through electrostatic interactions and π–π stacking interactions, making them a promising material for sensing specific biomolecular targets.[21] Although efficient MXene-based sensing of pesticides, phenol, glucose, and H_2O_2 have been reported,[22–24] no known work has explored the potential for structural modification of 2D nanosheet of MXenes to incorporate a high density of surface functional groups for electrochemical antibiotic sensing. However, planar surfaces of 2D MXenes could limit analytical performance and reduce dynamic range, leading to unstable immobilized probes and insufficient limits of detection (LOD) of antibiotics, making real-time monitoring challenging for biomarkers in the extracellular matrix (ECM) of human tissues.[25] Our innovation in this paper is to demonstrate that 2D nanosheets incorporated in 3D microstructures could provide high analytical performance and enable integration into implantable devices and *in vitro* analytical models. These 2D nanosheets in the 3D engineered structures enhance the electrode active surface area, and therefore, increase the biosensing signal. Moreover, due to excellent porosity of 3D architectures, there is potential to improve electrode reaction kinetics, reduce diffusion time, and increase interaction between the analyte and the specific immobilized probe, for improving sensing performance.

Considering the advantages of 3D structuring 2D MXenes, herein, we report 3D-printed microporous $Ti_3C_2T_X$ MXene sensors for monitoring antibiotic drug release in TES. The 3D microporous $Ti_3C_2T_X$ MXene is prepared by a simple dip coating of conductive 3D-printed acrylate-based polymer microlattices in MXene ink. Due to the 3D-printed microporous lattice structure bearing $Ti_3C_2T_X$ MXenes, effective ion intercalation and diffusivity is facilitated, resulting in excellent detection of antibiotics (i.e., gentamicin and vancomycin). The 3D microporous structure of $Ti_3C_2T_X$ MXene exposes more electrochemically active sensing surfaces, resulting in enhanced sensitivity for detecting gentamicin concentrations from 10 nM to 1 mM and vancomycin concentrations from 100 nM to 1 mM. We note that these limits of detection (LOD) are 1000 times more sensitive than those measured for planar 2D planar nanosheets of MXene. In addition, the suitability of the 3D microporous structure coated in $Ti_3C_2T_X$ MXene is characterized for bone tissue regeneration applications. Osteoblast-like (MG-63) cells are seeded on the 3D microporous $Ti_3C_2T_X$ MXene architecture, displaying promising biocompatibility and clinical translation potential of this technology. Thus, the incorporation of biocompatible 2D $Ti_3C_2T_X$

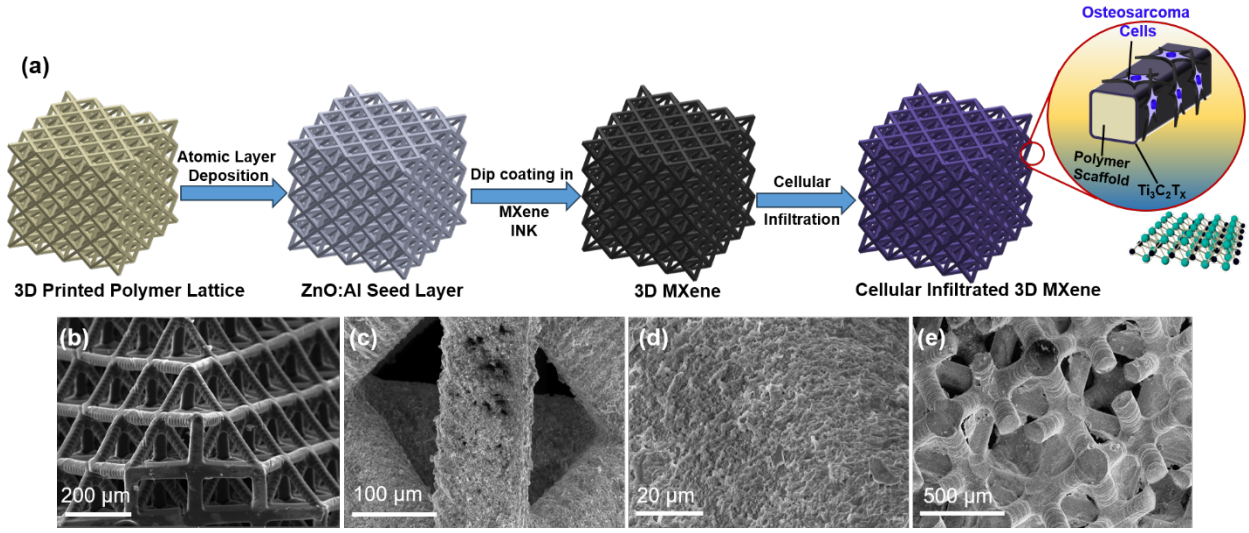

Figure 1. Synthesis and characterization of the 3D microporous $Ti_3C_2T_X$. a) Schematic illustration of the procedures for preparing the 3D microporous $Ti_3C_2T_X$ and illustration of the osteosarcoma cells proliferation on $Ti_3C_2T_X$. SEM images of the (b) 3D printed polymer lattice microstructure, (c) top view of 3D microporous $Ti_3C_2T_X$, and (d) high resolution of top view of 3D microporous $Ti_3C_2T_X$ coated lattice. e) Cross-sectional SEM image of 3D microporous lattice coated with $Ti_3C_2T_X$.

MXene into 3D microlattices provides a platform for directly integrating the current collector and sensing functions, enabling new applications for real-time monitoring of biomarkers in the ECM.

RESULTS AND DISCUSSION

Structural and Microstructural Characterization of 3D Microporous $Ti_3C_2T_X$ MXene

The intrinsic properties of $Ti_3C_2T_X$ MXene (i.e., quick absorption of aromatic compounds through electrostatic interactions, hydrophilicity, and biocompatibility) make it an ideal candidate for incorporation into 3D porous microstructures to develop 3D biosensors.[26] Moreover, our 3D structure utilizes the extremely high hydrophilicity and electronic properties of $Ti_3C_2T_X$ MXene that facilitate analyte diffusion while eliminating the need for additional binders and current collectors.[27] 3D microporous $Ti_3C_2T_X$ MXene is prepared by simple dip coating of 3D conducting polymer lattices into an aqueous MXene ink. Firstly, 3D polymer lattices are prepared by stereolithography (SLA) printing with a ultrahigh resolution acrylate-based resin (*UHR, Kudo*).[28,29] Conducting thin layers of ZnO:Al are then coated on these structures by atomic layer deposition (ALD) to improve the wettability of the 3D construct for MXene coating, according to procedures detailed in our previous work.[30] Finally, the as-prepared $Ti_3C_2T_X$ MXene nanosheets are coated by dipping the 3D lattices as detailed in the Experimental Section. The schematic illustration of the fabrication of 3D microporous $Ti_3C_2T_X$ MXene microlattice electrodes is shown in **Figure 1a,** and a detailed synthesis process of the MXene and the 3D-printed polymer lattices are described in the experimental section. Representative scanning electron microscopy (SEM)

images of the 3D microporous sensor structures are shown in **Figure 1b**. Note that a high magnification SEM image of 3D lattice structure is shown in the Supporting Information (**Figure S1**). Moreover, top and cross-sectional SEM images of the 3D microporous $Ti_3C_2T_X$ MXene are shown in **Figure 1c-e**. SEM images of the 3D microporous $Ti_3C_2T_X$ revealed continuous 3D structures with a micro porosity of 100 µm (**Figure 1c**), which falls in the optimal range for cell ingrowth and vascularization in these 3D structures[31]. The high-resolution SEM image of the 3D microporous $Ti_3C_2T_X$ shows a uniform continuous coating of 2D MXene sheets on the 3D structure (**Figure 1d**). Additionally, the cross-sectional SEM image of 3D microporous $Ti_3C_2T_X$ reveals that the microporous structure is fabricated without pore clogging or structural degradation (**Figure 1e**), indicating 3D microporous $Ti_3C_2T_X$ was prepared homogeneously. High-resolution cross-sectional SEM imaging of 3D microporous $Ti_3C_2T_X$ indicates the homogeneous coating of 2D MXene nanosheets on the inner surfaces of the porous 3D lattices (Supporting Information **Figure S2**), a critical feature to improve the overall biosensing performances of 3D microporous $Ti_3C_2T_X$.

To evaluate the crystal structures of as-synthesized $Ti_3C_2T_X$, X-ray diffraction (XRD) analysis was performed (**Figure 2a**). The black line (bottom) shows the diffraction pattern of MAX phase (Ti_3AlC_2). However, the diffraction pattern of $Ti_3C_2T_X$ MXene shows shift and broadening of (002) peak, confirming the etching of Al to form 2D nanosheets of $Ti_3C_2T_X$ MXene. The diffraction peak at 6.3 ° confirms the water intercalation in to the MXene sheets during washing process.[32] X-ray photoelectron spectroscopy (XPS) measurements were performed to characterize the chemical states of $Ti_3C_2T_X$ MXene, shown in **Figure 2b,c**. The survey spectrum of $Ti_3C_2T_X$ MXene confirms the presence of functional groups OH^-, O^{2-}, and F^{1-} along with metallic peaks of Ti and C (**Figure 2b**). **Figure 2c** shows the Ti 2p and C 1s core level spectra of $Ti_3C_2T_X$ MXene. In the Ti 2p result of $Ti_3C_2T_X$ MXene, there are three main peaks, labeled as Ti^{2+}, Ti–C, and Ti–O (Ti^{2+}: 454.7 eV, Ti–C: 455.9 eV, and Ti–O: 458.1 eV). The prominent peak at 461 eV belongs to 2 $p_{1/2}$ of Ti. The C 1s core level spectra shows two prominent peaks at 281.2 eV, and 284.2 eV, labeled as C-Ti-T_X, and C–C respectively, where T_X stands for terminating groups. It is noted from XPS analysis that C 1s spectra has metallic peaks confirming the metallic properties of $Ti_3C_2T_X$ MXene. We did not observe any impurity or Al peaks in $Ti_3C_2T_X$ MXene, confirming formation of $Ti_3C_2T_X$ MXene from MAX phase (Ti_3AlC_2). Atomic force microscopy (AFM) was used to obtain the thickness of exfoliated $Ti_3C_2T_X$ MXene, which was synthesized by sonication, shown in **Figure 2d**. It can be seen from AFM that exfoliated $Ti_3C_2T_X$ MXene has a thickness of ~3 nm, verifying that $Ti_3C_2T_X$ MXene consists of two layers (**Figure 2d)**.[33] The surface morphologies and nanostructures of the $Ti_3C_2T_X$ MXene are analyzed by transmission electron microscopy (TEM) and scanning electron microscopy (SEM). TEM image shows a semitransparent flake, confirming

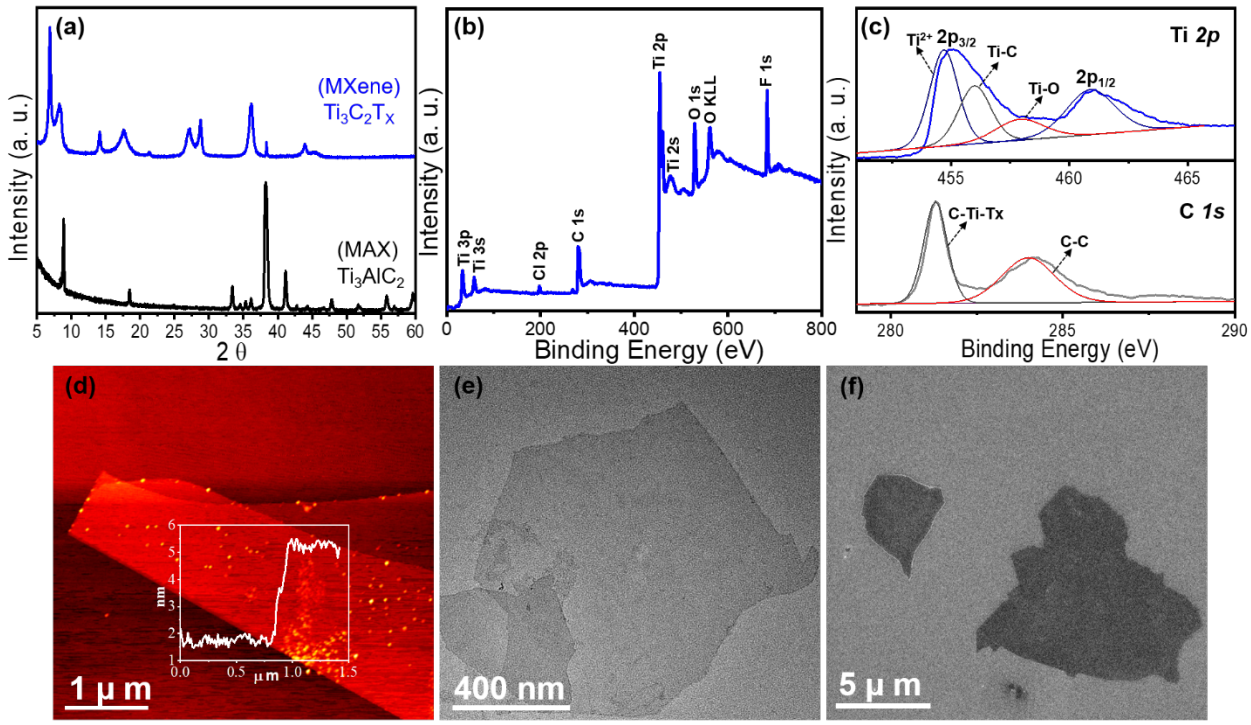

Figure 2. Structural characterization of $Ti_3C_2T_X$ MXene. a) XRD spectra of Ti_3AlC_2 (MAX) and $Ti_3C_2T_X$ MXene. XPS of $Ti_3C_2T_X$ MXene (b) survey spectra, (c) Ti 2p and C 1s core spectra. (d) AFM image of $Ti_3C_2T_X$ MXene with line scan shown in inset. (e) TEM image of $Ti_3C_2T_X$ MXene nanosheet. (f) SEM image of $Ti_3C_2T_X$ MXene nanosheet.

few or single layer $Ti_3C_2T_X$ MXene with a flake size of ~ 1 µm. A close look at the edges by high-resolution TEM (HRTEM) suggests that the $Ti_3C_2T_X$ MXene sheets primarily contain 2~3 layers (Supporting Information **Figure S3**), agreeing with AFM analysis. We can also observe that $Ti_3C_2T_X$ MXene shows an interlayer distance of 1.27 nm, which is in agreement with the XRD results. SEM images show $Ti_3C_2T_X$ MXene forming a distinct multilayered structure before the exfoliation process (Supporting Information **Figure S4**). High resolution SEM results (**Figure 2f**) further confirm the successful exfoliation of $Ti_3C_2T_X$ MXene into 2~3-layer sheets with a lateral size of ~5 µm, confirming the synthesis of high-quality few layer 2D MXene.

Antibiotic Sensing Performance of 3D Microporous $Ti_3C_2T_X$ MXene

Using our 3D microporous $Ti_3C_2T_X$ MXene as a working electrode, we demonstrate sensitive detection of antibiotics via amperometry using a standard three-electrode configuration, with a Pt wire as counter electrode (CE) and a reference electrode (RE) of Ag/AgCl. The redox reaction involves the oxidation of antibiotics in DI water and/or buffer electrolyte on the surface of the working electrode (WE) (3D microporous $Ti_3C_2T_X$ MXene); therefore, the redox current can be monitored to detect the concentration of antibiotics (**Figure 3a**).[34] The performance of our fabricated 3D microporous $Ti_3C_2T_X$ MXene biosensors is evaluated at room temperature. As

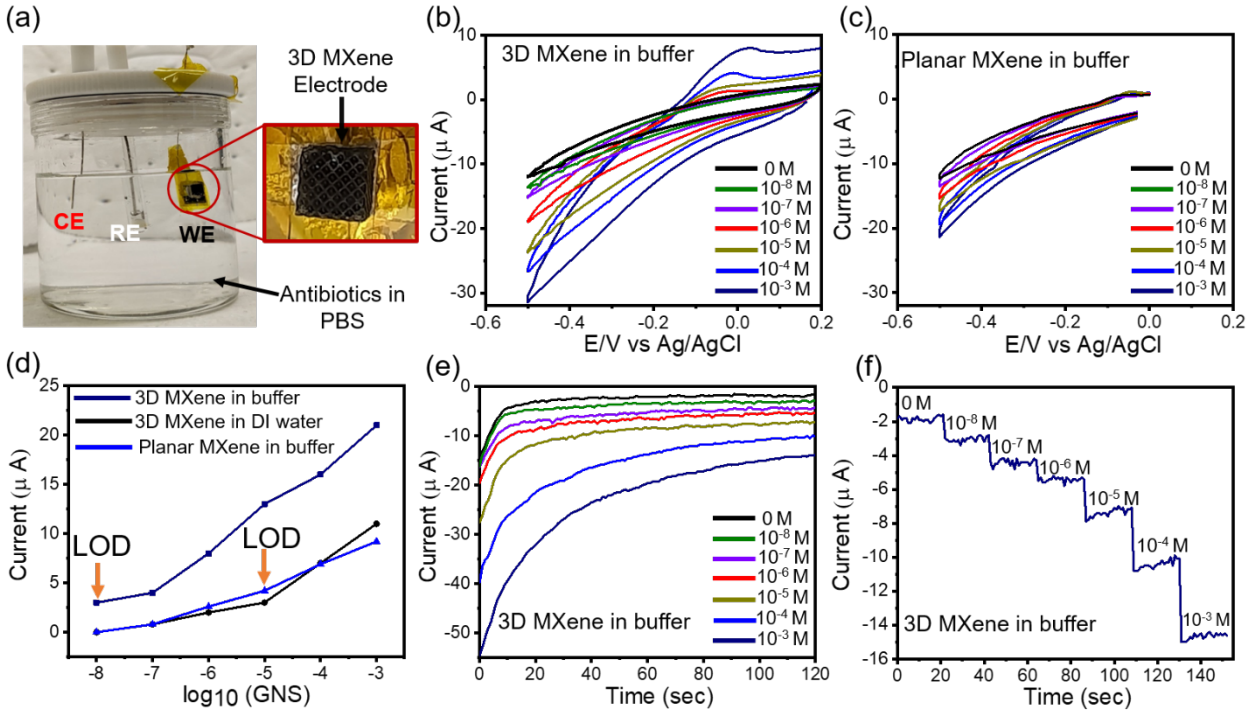

Figure 3. Biosensing performance of the 3D microporous $Ti_3C_2T_X$ for gentamycin. a) Real image of electrochemical cell for antibiotic sensing. Cyclic voltammetry (b) for 3D microporous $Ti_3C_2T_X$ MXene, and (c) for planar films of $Ti_3C_2T_X$ MXene. (d) Calibration graphs to know the detection limits. (d) Chronoamperometry of 3D microporous $Ti_3C_2T_X$ MXene. (f) Real time detection graph for 3D microporous $Ti_3C_2T_X$ MXene.

shown in **Figure 3b**, an oxidation potential of approximately 13 mV (vs. Ag/AgCl) was determined through cyclic voltammetry (CV) by measuring the response current between the 3D microporous $Ti_3C_2T_X$ | MXene and Pt wire in the presence of 10^{-3} M gentamycin in buffer solution (PBS). **Figure 3b** shows the gentamycin concentration dependence of the current response measured through cyclic voltammetry (CV). As the gentamycin concentration decreases, a decrease in the current response and a shift in oxidation potential to higher potentials was observed. Moreover, the oxidation peak eventually disappeared when the concentration of gentamycin reached 10^{-8} M in buffer solution. Notably, no oxidation peak was observed in the CV results of planar $Ti_3C_2T_X$ MXene samples lacking the 3D microstructure, confirming that planar sheets of $Ti_3C_2T_X$ MXene alone do not provide sufficient active sites for efficient redox of gentamycin (**Figure 3c**). Similar trends are seen in the biosensing performance of 3D microporous $Ti_3C_2T_X$ MXene in DI water, (Supporting Information **Figure S5**) particularly because of the lower ionic concentration of DI water compared to the PBS. To confirm the influence of the MXene coating on biosensing, we performed CV on microlattices coated only in ZnO:Al. It was observed that ZnO:Al coated polymer microlattice exhibited 10 times lower current response than 3D $Ti_3C_2T_X$ MXene (Supporting Information **Figure S6**), confirming the importance of $Ti_3C_2T_X$ MXene for performing efficient biosensing. **Figure 3d** shows the calibration graphs to determine the

detection limits of biosensors for gentamycin incorporated with 3D microporous $Ti_3C_2T_X$ MXene in buffer, $Ti_3C_2T_X$ MXene in DI water, and planar $Ti_3C_2T_X$ MXene in buffer. 3D microporous $Ti_3C_2T_X$ MXene is able to sense gentamycin at the best (lowest) LOD (10^{-8} M of gentamycin in buffer) compared with the planar $Ti_3C_2T_X$ MXene sensors (LOD of 10^{-5} M for gentamycin in buffer). Our 3D sensors achieve lower LOD when compared with reported nanomaterial-based biosensors for gentamycin at -0.4 V (vs. Ag/AgCl).[35] The time-dependent current response at different gentamycin concentrations was measured through chronoamperometry (**Figure 3e, f**). At low gentamycin concentrations of less than 100 μM, the current response stabilizes within approximately 10 s, which is important for achieving real-time gentamycin monitoring. Larger concentrations produce an extended response stabilizing over the course of approximately 100 s. Notably, planar films of $Ti_3C_2T_X$ MXene showed two times lower current response than 3D microstructure $Ti_3C_2T_X$ MXene at same voltage (Supporting Information **Figure S7**), confirming less active sites on planar films of $Ti_3C_2T_X$ MXene. As shown in **Figure 3f**, the introduction of increasing gentamycin concentrations across a broad range from 10 nM to 1 mM can be detected at 20 s intervals, which is similar to the detection limit estimated by CV measurements. To determine the intrinsic kinetic characteristics of 3D microstructure $Ti_3C_2T_X$ MXene, we measured charge transfer resistance (R_{ct}) by electrochemical impedance spectroscopy (EIS). It was found that 3D microstructure $Ti_3C_2T_X$ MXene possessed 10 times lower R_{ct} (20 Ω) than only ZnO:Al coated 3D microstructure (~200 Ω) (Supporting Information **Figure S8**), confirming the importance of MXene for efficient biosensing.

To understand the generality of the sensing function of 3D microporous $Ti_3C_2T_X$ MXene, detection of a second antibiotic (vancomycin) commonly used in bone grafts was characterized by redox current measurements (CV and chronoamperometry). As shown in **Figure 4a**, an oxidation potential of approximately -0.3 V (vs. Ag/AgCl) was determined for the 3D microporous $Ti_3C_2T_X$ MXene in the presence of 10^{-3} M vancomycin in buffer solution. Similar to gentamycin, with decreases in concentration of vancomycin, a decrease in the magnitude of the current response is observed. Notably, contrary to gentamycin, there was no shift observed in the oxidation potential, perhaps because of the higher content of hydroxyl groups in vancomycin compared with gentamycin. Interestingly, reduction peaks are observed in the CV characteristics for vancomycin sensing at -0.3 V (vs. Ag/AgCl), confirming the redox reaction of vancomycin on 3D microporous $Ti_3C_2T_X$ MXene. Notably, no peaks of oxidation and/or reduction are observed in planar $Ti_3C_2T_X$ MXene, indicating planar $Ti_3C_2T_X$ MXene may not be able to provide sufficient active sites to redox vancomycin (**Figure 4b**). Calibration graphs of biosensors for vancomycin via 3D microporous $Ti_3C_2T_X$ MXene, and planar $Ti_3C_2T_X$ MXene in buffer are plotted to determine the

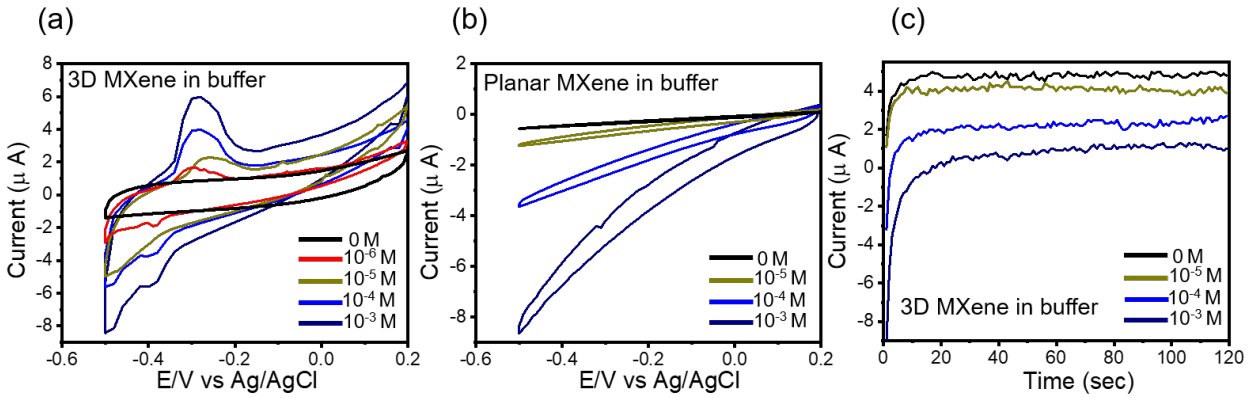

Figure 4. Biosensing performance of the 3D microporous $Ti_3C_2T_X$ for vancomycin. Cyclic voltammetry a) for 3D microporous $Ti_3C_2T_X$ MXene, and (b) for planar $Ti_3C_2T_X$ MXene. c) Chronoamperometry measurements of 3D microporous $Ti_3C_2T_X$ MXene.

detection limits (shown in Supporting Information **Figure S9**). 3D microporous $Ti_3C_2T_X$ MXene shows a sensing detection limit of 10^{-7} M for vancomycin, which is 100 times better than planar $Ti_3C_2T_X$ MXene (10^{-5} M) in buffer at -0.3 V (vs. Ag/AgCl), and better than reported electrochemical biosensors for vancomycin.[36] Chronoamperometry results for vancomycin detection show similar trends as CV curves with detection limit 10^{-7} M in buffer (**Figure 4c**).

To generalize the practical applications of 3D microporous $Ti_3C_2T_X$ MXene biosensors, we characterized the sensing performance in relevant physiological environments emulating chemical features of the human immune response, including elevated temperatures and increased H_2O_2 concentrations.[37] With increasing the temperature from room temperature to 37 °C, lower current response of the oxidation of gentamycin is detected due to lower oxidation of gentamycin in buffer at higher temperature. However, the oxidation peaks are sufficient to detect the gentamycin at elevated temperatures (35, 36, and 37 °C) (shown in Supporting Information **Figure S10a**). Similar trends are observed in detection of vancomycin at elevated temperatures. Notably, the oxidation peak shift is observed towards lower potentials in vancomycin detection, confirming lower potential is needed to detect vancomycin at elevated temperatures (shown in Supporting Information **Figure S10b**). To test the impact of H_2O_2 on sensor performance, a concentration of 10^{-3} M of both gentamycin and vancomycin was injected while observing the response of the 3D microporous $Ti_3C_2T_X$ MXene biosensors. In both cases the oxidation peaks disappear due to the presence of H_2O_2 because H_2O_2 hinders the oxidation of antibiotics. However, the current response magnitude is retained, allowing similar detection of antibiotics in environments with H_2O_2 (shown in Supporting Information **Figure S11**). It is noted that in relevant physiological environments, detection of antibiotics can still be observed, nevertheless. Further improvement of the sensitivity could be achieved by depositing a higher amount of MXene, though this may sacrifice the detection limit to a certain extent. Importantly, in addition to the superior biosensing of 3D microporous $Ti_3C_2T_X$ MXene showed outstanding stability, exhibiting constant saturation current during a

chronoamperometry test up to 16 hours, performed at -0.5 V in PBS (shown in Supporting Information **Figure S12**).

Biocompatibility of 3D Microporous $Ti_3C_2T_X$ MXene

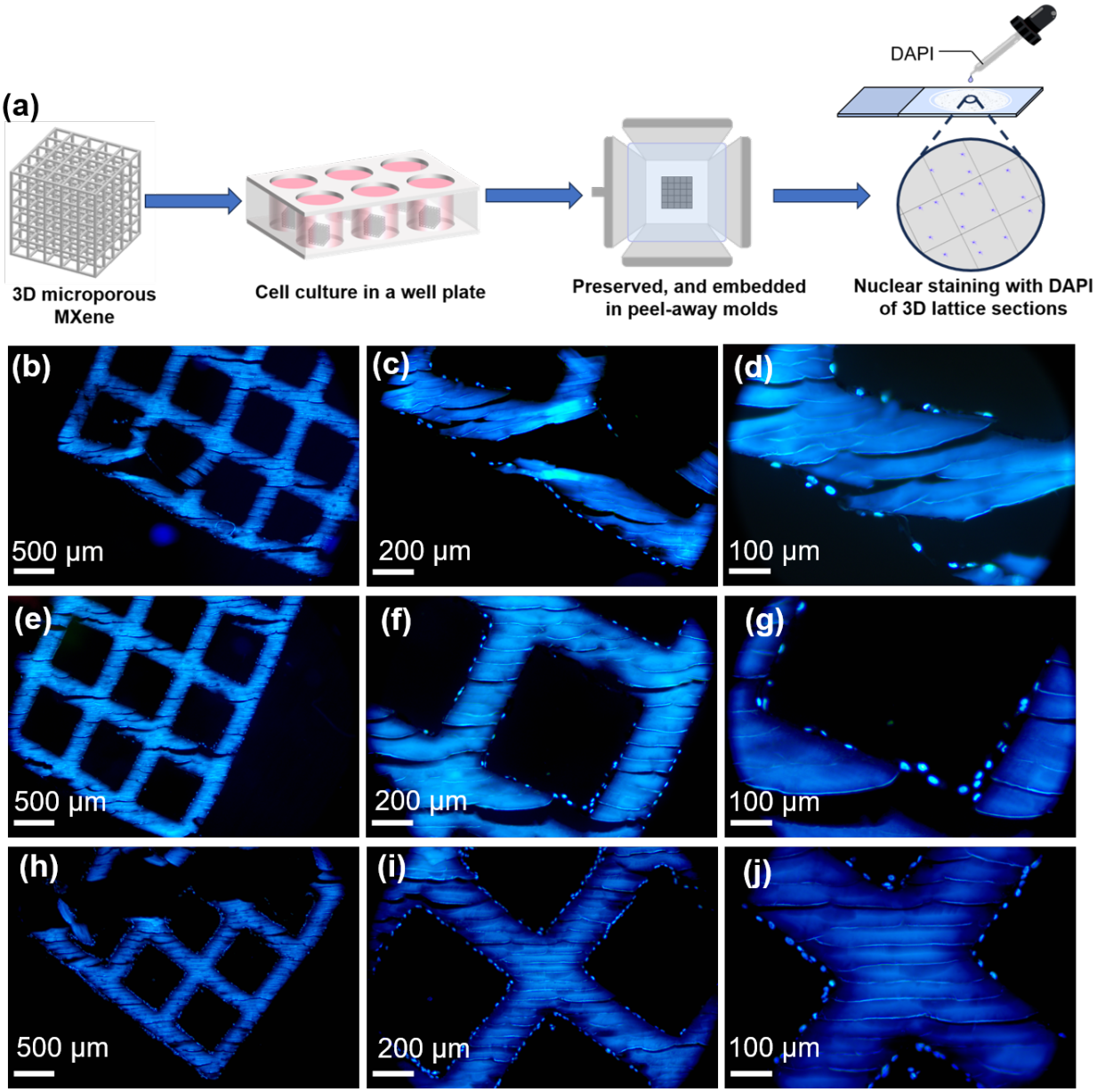

Figure 5. Biocompatibility of $Ti_3C_2T_X$ MXene and Cellular Infiltration. a) Schematic illustration of sample preparation for biocompatibility test. The 3D lattices are taken from culture, preserved, and embedded in peel-away molds. Sections of the 3D lattices are then taken using a cryostat followed by nuclear staining with 4′,6-Diamidino-2-phenylindole dihydrochloride and imaged under a fluorescence microscope. Cellular infiltration of cubic MXene lattice after (b) three days of culture at 4x magnification (c) 10x magnification, and (d) 20x magnification. (e) Cellular infiltration after five days of culture at 4x magnification, (f) 10x magnification, and (g) 20x magnification. (h) Cellular infiltration after seven days of culture at 4x magnification, (i) 10x magnifications, and (j) 20x magnification.

Towards the goal of engineering an implantable sensor compatible with TES, we studied the biocompatibility of our 3D MXene coated microstructures via cell attachment and infiltration. Our findings revealed that there was no significant cytotoxicity observed for MG63s cells after incubation with 3D microporous $Ti_3C_2T_X$ MXene. To assess the biocompatibility of 3D microporous $Ti_3C_2T_X$ MXene, human osteosarcoma (MG63, passage 95; ATCC) cells were applied by slowly dripping 100 µL of cell suspension on the top of the microlattice (**Figure 5a**) (details are explained in experimental section). As culture time of MG63s on the MXene coated lattice structures increased, cellular growth and proliferation also increased from Day 3 to 7. Cellular aggregation on the microlattice structures is polarized to areas with MXene deposition and interior infiltration can be seen to increase over the course of the study. Most notably, it can be seen from **Figure 5h-j** that cell infiltration has quickly shifted towards the interior and surfaces coated with MXene have become lined with the osteoblast-like cells. In contrast, cubic lattice structures made with the same polymer resin that did not receive MXene coating did not yield any cellular infiltration, growth or proliferation after 7 days of culture (**Figure S13**). While toxicity has been considered in other studies regarding MXene, no known studies have looked at evaluating cellular proliferation or infiltration within scaffolds using MG63 cells.[38] Some studies have shown good cytocompatibility and cell viability at various concentrations of $Ti_3C_2T_X$ MXene with myoblast (C2C12), endothelial (HUVEC), and other osteosarcoma (Saos2) cell lines.[39,40]

CONCLUSION

We report a 3D microporous $Ti_3C_2T_X$ MXene-based implantable electrochemical antibiotic sensor with a wide sensing range for gentamicin concentrations from 10 nM to 1 mM, and vancomycin concentrations from 100 nM to 1 mM, a low detection limit (10 nM), and a response time of less than 10 s. Compared with typical planar film sensors, our work demonstrates that 3D-printed microporous structures can offer enhanced sensing performance for continuous monitoring in physiologically relevant environments. We further investigated the biocompatibility of these 3D printed structures, showing the clinical translation potential for integrating 3D microporous $Ti_3C_2T_X$ MXene sensors with implantable tissue engineering scaffolds for *in vivo* applications. This 3D microporous $Ti_3C_2T_X$ MXene architecture has the potential to provide a platform for mediator-free biosensing, enabling new applications for *in vivo* monitoring of drug elution. These results provide a strategy for integrating electrical biosensing functions directly into implantable biomaterials via 3D-printing, a first step towards closed loop control of drug delivery.

Experimental Section

Preparation of 3D microporous $Ti_3C_2T_X$ MXene microlattices

The 3D polymer lattices were printed using a Kudo3D stereolithography system with Ultra High Resolution (UHR) positive resin. The 3D polymer lattice microstructures were then coated with conductive ZnO:Al by atomic layer deposition (ALD). For further details of 3D polymer printing and the ALD 3D coating processes, please see our recent publications.[28] To complete the sensitization of the 3D microporous $Ti_3C_2T_X$ MXene microstructures, dip coating was performed by applying ultra-sonication to the solution while submerging the lattice. $Ti_3C_2T_x$-MXene materials were synthesized through an acid (HF + HCl) etching method of the MAX phase (Ti_3AlC_2). Details of this specific MXene synthesis can be seen in our recent publication.[41] The $Ti_3C_2T_x$-MXene solution with a concentration of 1 mg mL^{-1} was obtained by sonication for 30 min. Lastly, the ALD-coated 3D polymer lattice microstructure was submerged in the MXene solution and sonicated for 30 min. The MXene coated 3D polymer microlattice was then dried in a vacuum oven at 60 °C for 1 hour.

Chemical and Microstructural Characterization

The microstructures of the planar MXene, and 3D microporous $Ti_3C_2T_X$ MXene were analyzed by transmission electron microscopy (TEM) (JEOL, 300 KV), and scanning electron microscopy (SEM) (Helios 660). The crystal structure of the MXene was determined by powder X-ray diffraction (XRD) (Rigaku, Miniflex). The chemical composition of the 3D $Ti_3C_2T_X$ MXene was investigated by X-ray photospectroscopy (XPS) (Kratos, Axis Supra XPS).

Electrochemical Biosensing

Electrochemical biosensing experiments were performed with a VersaSTAT 3 (*Princeton Applied Research*) electrochemical setup with a three-electrode system. Electrochemical tests were performed in different concentration of antibiotic in water or PBS, as noted. The working electrode was a 3D microporous $Ti_3C_2T_X$ MXene lattice, the reference electrode was Ag/AgCl in 3M KCl, and the counter electrode was a Pt wire. The control electrochemical tests were completed in neat PBS electrolyte with no antibiotic to attain a baseline current response. The detection limit was obtained by monitoring the current response of the electrodes. When the current response to the antibiotic in PBS was observed to be similar to that of neat PBS, the concentration was considered to be at the limit of detection (LOD).

Cell Studies Characterizing Biocompatibility of 3D microporous $Ti_3C_2T_X$ MXene

MXene-coated lattice microstructures were sterilized in 70% EtOH for 30 minutes followed by three consecutive 10 minute washes in sterile 1X phosphate-buffered-saline (PBS). After sterilization, each lattice microstructure was seeded with 50,000 human osteosarcoma (MG63, passage 95; ATCC) cells by slowly dripping 100 µL of cell suspension on the top of the structure. Cells were cultured in growth medium composed of Dulbecco's Modified Eagle Medium (DMEM)

supplemented with 4.5 g/L Glucose, L-Glutamine, and 110 mg/L sodium pyruvate (Gibco), 10% fetal bovine serum (Omega Scientific), and 1% penicillin-streptomycin solution (Gibco). The seeded lattices were incubated for one hour at 37°C and 5% CO2 to allow for cellular attachment. Thereafter, 1.5 mL of media was added so that the structures were submerged. Media was replaced every two-to-three days and samples were removed at days 3, 5, and 7. Upon removal, samples were placed in formalin for 24 hours for preservation and subsequently cryoprotected with 30% (w/v) sucrose (Sigma-Aldrich) for 24 hours. To embed the samples, a 5% (w/w) porcine gelatin (Sigma-Aldrich) and 5% (w/w) sucrose solution was dissolved in deionized water and pre-warmed to 45°C. The samples were then placed in molds, embedding solution was pipetted into the molds, and all samples were incubated for 2 hours at 45°C. Once complete, molds were subsequently immersed in an acetone and dry ice bath until frozen. The samples were transferred to a -80°C freezer until they were ready to be sectioned. Cryosectioning was completed at -20°C, and all sections were taken between 16-20 μm and stained with 4′,6-diamidino-2-phenylindole, dihydrochloride (DAPI; BD Biosciences). Images were taken by an inverted compound light microscope (Laxco SLi3PRO Inverted Fluorescence Microscope) at 4x, 10x, and 20x magnification.

REFERENCES

[1] R. Finkel (PharmD.), M. A. Clark, L. X. Cubeddu, *Pharmacology*, Lippincott Williams & Wilkins, **2009**.

[2] C. Whisstock, A. Volpe, S. Ninkovic, M. Marin, M. Meloni, M. Bruseghin, G. Boschetti, E. Brocco, *Journal of Clinical Medicine* **2020**, *9*, 3586.

[3] P. Coimbra, J. P. Freitas, T. Gonçalves, M. H. Gil, M. Figueiredo, *Materials Science and Engineering: C* **2019**, *94*, 86.

[4] H. Kyriacou, A. Kamaraj, W. S. Khan, *Applied Sciences* **2020**, *10*, 2244.

[5] C. Zhao, W. Liu, M. Zhu, C. Wu, Y. Zhu, *Bioactive Materials* **2022**, *18*, 383.

[6] Z. Gholami, S. Hasanpour, S. Sadigh, S. Johari, Z. Shahveghar, K. Ataei, E. Javari, M. Amani, L. Javadi Kia, Z. Delir Akbari, Z. Nazari, S. Maleki Dizaj, Y. Rezaei, *J Adv Periodontol Implant Dent* **2021**, *13*, 43.

[7] V. J. Antoci, C. S. Adams, N. J. Hickok, I. M. Shapiro, J. Parvizi, *Clinical Orthopaedics and Related Research®* **2007**, *462*, 200.

[8] H. P. Dang, T. Shabab, A. Shafiee, Q. C. Peiffer, K. Fox, N. Tran, T. R. Dargaville, D. W. Hutmacher, P. A. Tran, *Biofabrication* **2019**, *11*, 035014.

[9] C. Wang, W. Huang, Y. Zhou, L. He, Z. He, Z. Chen, X. He, S. Tian, J. Liao, B. Lu, Y. Wei, M. Wang, *Bioactive Materials* **2020**, *5*, 82.

[10] E. Kaale, S. Leonard, A. Van Schepdael, E. Roets, J. Hoogmartens, *Journal of Chromatography A* **2000**, *895*, 67.

[11] A.-S. Fiolet, E. Jandot, P. Doucey, C. Crétet, C. Brunel, C. Pivot, J.-M. Ghigo, C. Beloin, D. Lebeaux, F. Pirot, *J Pharm Anal* **2018**, *8*, 386.

[12] M. A. Omar, D. M. Nagy, M. A. Hammad, A. A. Aly, *J App Pharm Sci* **2013**, *3,* 151.

[13] P. Singh, K. Sharma, V. Hasija, V. Sharma, S. Sharma, P. Raizada, M. Singh, A. K. Saini, A. Hosseini-Bandegharaei, V. K. Thakur, *Materials Today Chemistry* **2019**, *14*, 100186.
[14] E. Khaled, M. M. Khalil, G. M. Abed el Aziz, *Sensors and Actuators B: Chemical* **2017**, *244*, 876.
[15] F. Luan, Y. Wang, S. Zhang, X. Zhuang, C. Tian, X. Fu, L. Chen, *Analyst* **2020**, *145*, 1943.
[16] F. Meng, H. Sun, Y. Huang, Y. Tang, Q. Chen, P. Miao, *Analytica Chimica Acta* **2019**, *1047*, 45.
[17] M. M. Khalil, G. M. A. El-aziz, *Electroanalysis* **2017**, *29*, 566.
[18] B. Anasori, Y. Xie, M. Beidaghi, J. Lu, B. C. Hosler, L. Hultman, P. R. C. Kent, Y. Gogotsi, M. W. Barsoum, *ACS Nano* **2015**, *9*, 9507.
[19] Y. Yoon, T. Anh Le, A. P. Tiwari, I. Kim, M. W. Barsoum, H. Lee, *Nanoscale* **2018**, *10*, 22429.
[20] Y. Yoon, A. P. Tiwari, M. Choi, T. G. Novak, W. Song, H. Chang, T. Zyung, S. S. Lee, S. Jeon, K.-S. An, *Advanced Functional Materials* **2019**, *29*, 1903443.
[21] M. Mathew, C. S. Rout, *Current Opinion in Electrochemistry* **2021**, *30*, 100782.
[22] L. Lorencova, T. Bertok, E. Dosekova, A. Holazova, D. Paprckova, A. Vikartovska, V. Sasinkova, J. Filip, P. Kasak, M. Jerigova, D. Velic, K. A. Mahmoud, J. Tkac, *Electrochimica Acta* **2017**, *235*, 471.
[23] H. Liu, C. Duan, C. Yang, W. Shen, F. Wang, Z. Zhu, *Sensors and Actuators B: Chemical* **2015**, *218*, 60.
[24] H. L. Chia, C. C. Mayorga-Martinez, N. Antonatos, Z. Sofer, J. J. Gonzalez-Julian, R. D. Webster, M. Pumera, *Anal. Chem.* **2020**, *92*, 2452.
[25] T. Bertok, A. Sediva, A. Vikartovska, J. Tkac, *Int J Electrochem Sci* **2014**, *9*, 890.
[26] Z. Yang, J. Hu, X. Zhang, H. Yang, P. Meng, H. Zhao, Y. Sun, *Anal Bioanal Chem* **2023**, *415*, 157.
[27] H.-P. Li, J. Wen, S.-M. Ding, J.-B. Ding, Z.-H. Song, C. Zhang, Z. Ge, X. Liu, R.-Z. Zhao, F.-C. Li, *Nano Materials Science* **2023**, DOI 10.1016/j.nanoms.2023.02.001.
[28] J. E. Huddy, W. J. Scheideler, *STAR Protocols* **2022**, *3*, 101523.
[29] J. E. Huddy, A. P. Tiwari, H. Zhao, Y. Li, W. J. Scheideler, *Advanced Materials Technologies* **n.d.**, *n/a*, 2300180.
[30] J. E. Huddy, M. S. Rahman, A. B. Hamlin, Y. Ye, W. J. Scheideler, *Cell Reports Physical Science* **2022**, *3*, 100786.
[31] N. Abbasi, S. Hamlet, R. M. Love, N.-T. Nguyen, *Journal of Science: Advanced Materials and Devices* **2020**, *5*, 1.
[32] M. Ghidiu, S. Kota, V. Drozd, M. W. Barsoum, *Science Advances* **2018**, *4*, eaao6850.
[33] Y. Yoon, A. P. Tiwari, M. Lee, M. Choi, W. Song, J. Im, T. Zyung, H.-K. Jung, S. Sook Lee, S. Jeon, K.-S. An, *Journal of Materials Chemistry A* **2018**, *6*, 20869.
[34] M. Imran, S. Ahmed, A. Z. Abdullah, J. Hakami, A. A. Chaudhary, H. A. Rudayni, S.-U.-D. Khan, A. Khan, N. S. Basher, *Luminescence* **2023**, *38*, 1064.
[35] E. Khaled, M. M. Khalil, G. M. Abed el Aziz, *Sensors and Actuators B: Chemical* **2017**, *244*, 876.
[36] B. Feier, A. Blidar, L. Vlase, C. Cristea, *Electrochemistry Communications* **2019**, *104*, 106474.
[37] W. Razzell, I. R. Evans, P. Martin, W. Wood, *Current Biology* **2013**, *23*, 424.

[38] J. Wu, Y. Yu, G. Su, *Nanomaterials* **2022**, *12*, 828.
[39] X. Qu, Y. Guo, C. Xie, S. Li, Z. Liu, B. Lei, *ACS Nano* **2023**, *17*, 7229.
[40] S. Pan, J. Yin, L. Yu, C. Zhang, Y. Zhu, Y. Gao, Y. Chen, *Advanced Science* **2020**, *7*, 1901511.
[41] A. P. Tiwari, S. McBride, A. B. Hamlin, M. S. Rahman, J. E. Huddy, G. Hautier, W. J. Scheideler, *ACS Sustainable Chem. Eng.* **2023**, *11*, 12084.

Supporting Information

Biocompatible 3D-Printed MXene microlattices for tissue-integrated antibiotic sensing

*Anand P. Tiwari, Sreejith S. Panicker, Julia E. Huddy, Md Saifur Rahman, Katherine R. Hixon, and William J. Scheideler**

Thayer School of Engineering, Dartmouth College, Hanover, NH 03755, USA.

Email: william.j.scheideler@dartmouth.edu

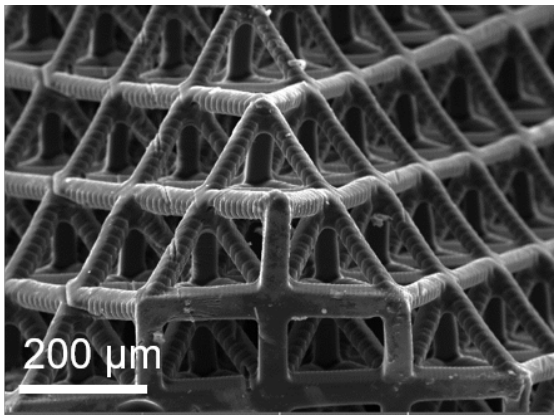

Fig. S1 SEM image of 3D-printed octet structured polymer microlattice.

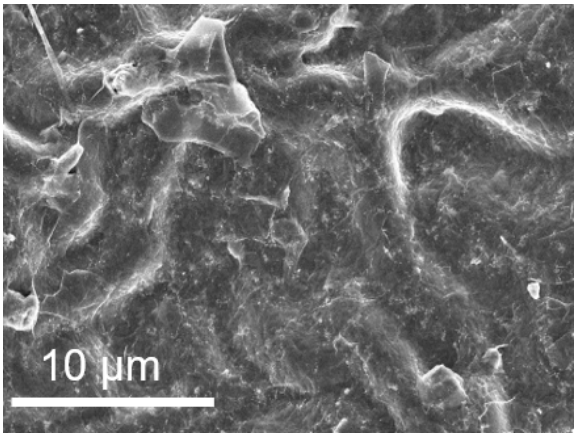

Fig. S2 High resolution cross-sectional SEM image of $Ti_3C_2T_X$ MXene coating on the surface of 3D microlattices.

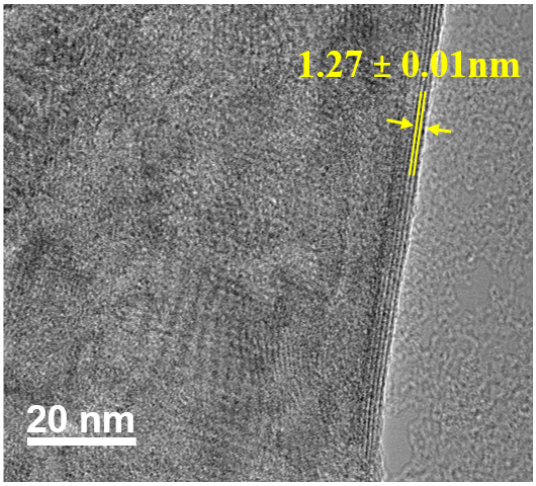

Fig. S3 High resolution TEM image of $Ti_3C_2T_X$ MXene.

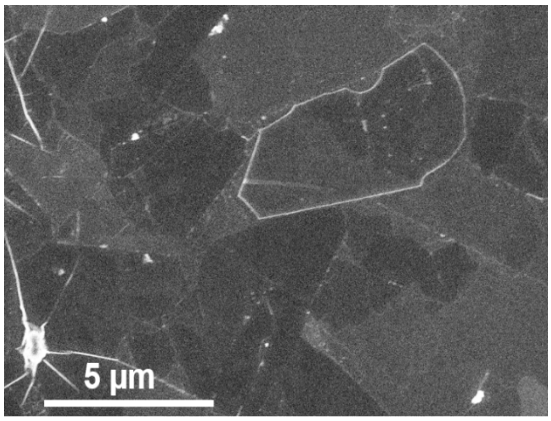

Fig. S4 SEM image of $Ti_3C_2T_X$ MXene flakes before exfoliation.

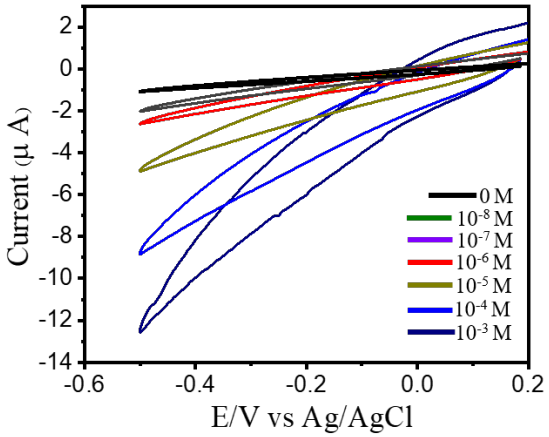

Fig. S5 Cyclic voltammetry measurements of biosensing performance of the 3D microporous $Ti_3C_2T_X$ microlattices for detection of gentamycin in DI water.

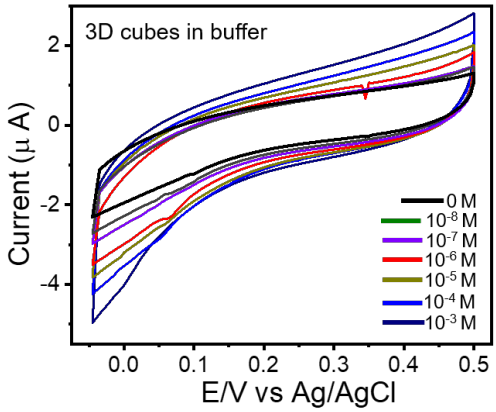

Fig. S6 Cyclic voltammetry measurements of biosensing performance of ZnO:Al coated microlattices for detection of gentamycin in PBS.

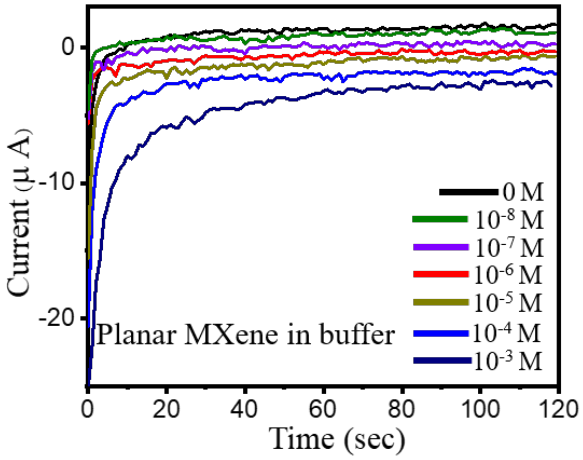

Fig. S7 Chronoamperometry measurements of planar films of $Ti_3C_2T_X$ MXene for detection of gentamycin in buffer solution (PBS).

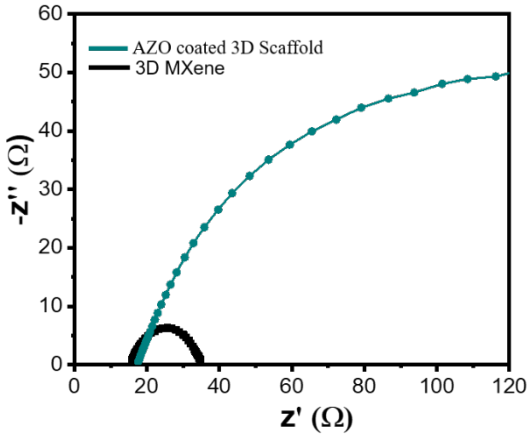

Fig. S8 Nyquist plot used to determine the charge transfer resistance of 3D $Ti_3C_2T_X$ MXene, and ZnO:Al-coated 3D microlattices in buffer solution (PBS).

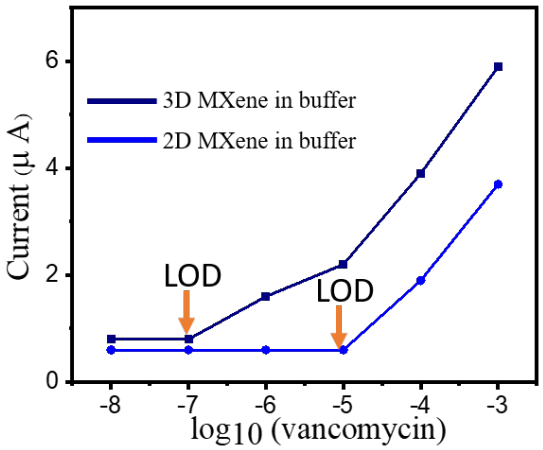

Fig. S9 Calibration graphs used to determine the limits of detection (LOD) for vancomycin in buffer solution (PBS).

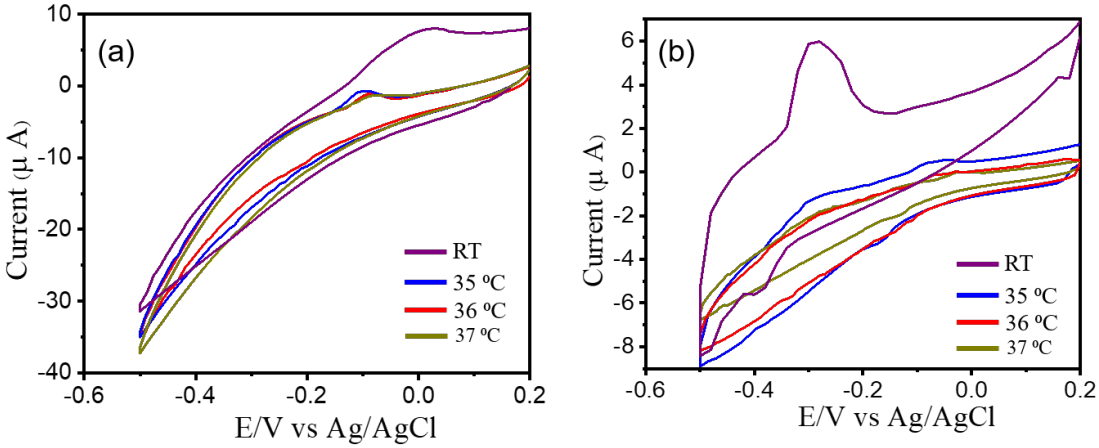

Fig. S10 Temperature dependent cyclic voltammetry measurements of biosensing performance of the 3D microporous $Ti_3C_2T_X$ for detection of (a) gentamycin and (b) vancomycin in buffer solution (PBS).

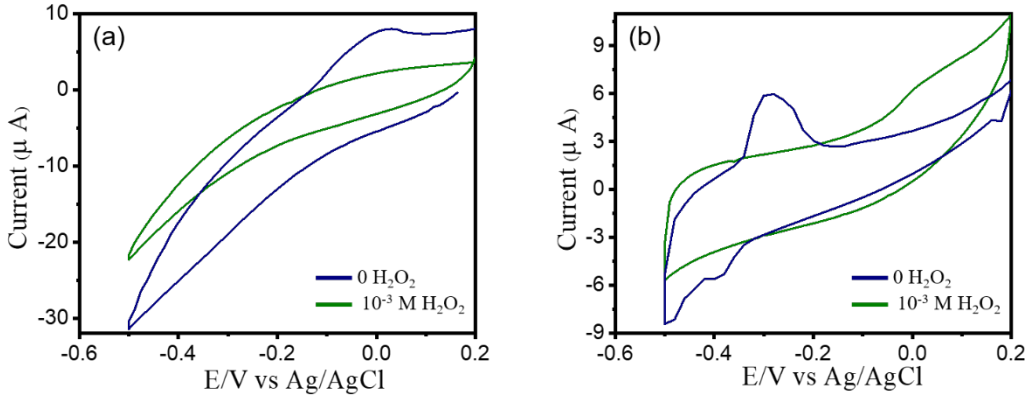

Fig. S11 H_2O_2 concentration-dependent biosensing performance of the $Ti_3C_2T_X$ 3D microlattices for detection of (a) gentamycin and (b) vancomycin in buffer solution (PBS).

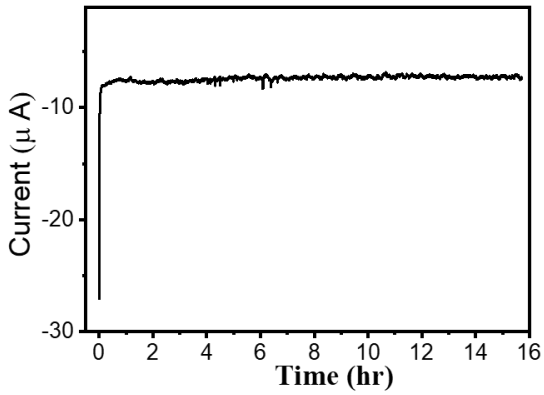

Fig. S12 Long-term chronoamperometry measurements of 3D $Ti_3C_2T_X$ MXene microlattices submerged in buffer solution (PBS).

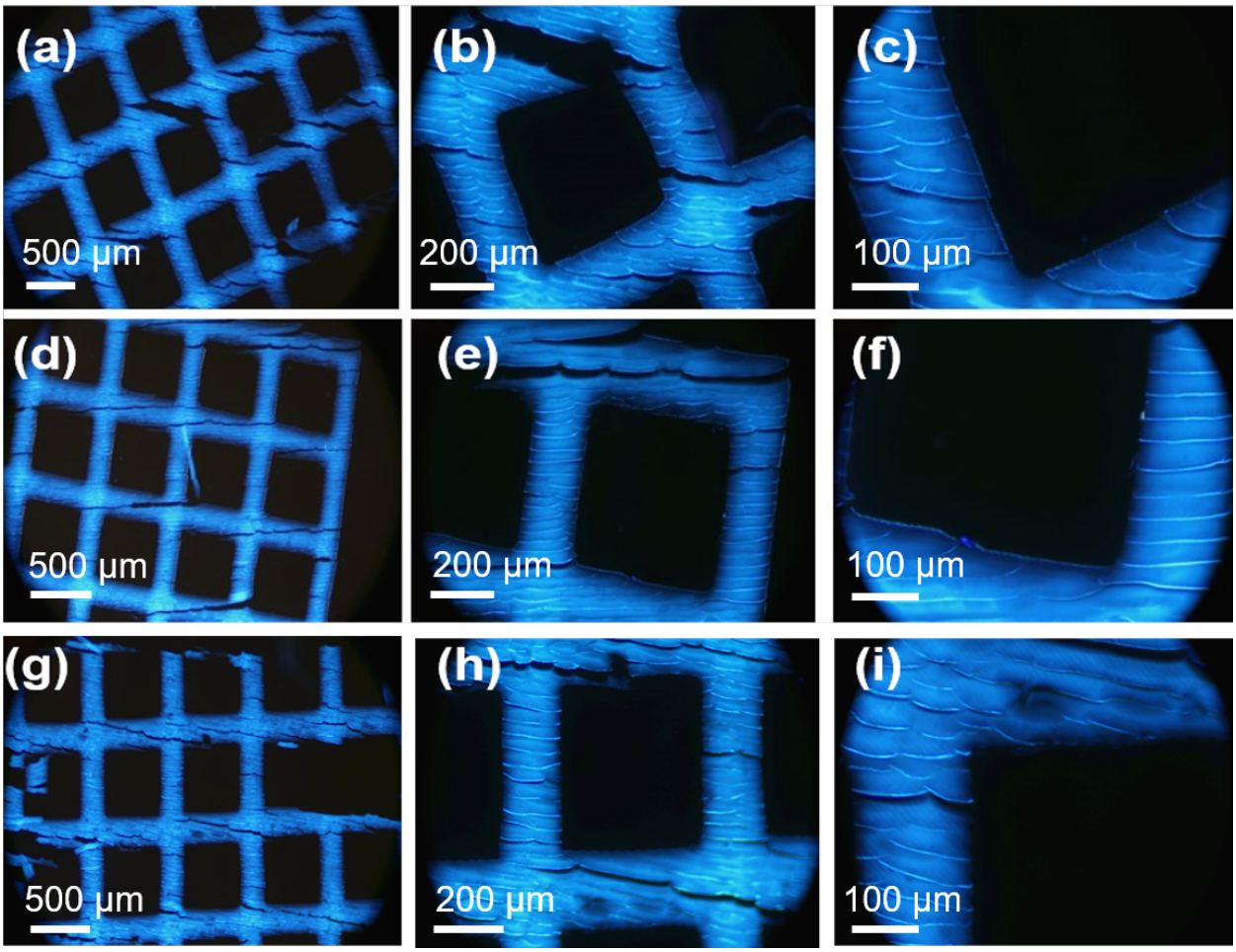

Fig. S13 Cellular infiltration of cubic microlattices with no MXene coating after (a) three days of culture at 4x magnification (b) 10x magnification, and (c) 20x magnification. (d) Cellular infiltration after five days of culture at 4x magnification, (e) 10x magnification, and (f) 20x magnification. (g) Cellular infiltration after seven days of culture at 4x magnification, (h) 10x magnifications, and (i) 20x magnification.